JOURNAL OF AIRCRAFT
Vol. 43, No. 5, September–October 2006

Effect of Flap and Slat Riggings on 2-D High-Lift Aerodynamics

R. Balaji,* F. Bramkamp,† M. Hesse,‡ and J. Ballmann§
Rheinisch–Westfälische Technische Hochschule Aachen, 52056 Aachen, Germany

DOI: 10.2514/1.19391

In this paper an extensive parametric study concerning the effect of flap and slat riggings on the 2-D high-lift flow past a three-element airfoil system is presented. The numerical approach for solving the Reynolds-averaged Navier–Stokes equations uses an implicit finite volume scheme of second order accuracy in space on a patched multizonal grid. The Spalart–Allmaras one-equation turbulence model is employed. Six design parameters have been investigated comprising the deviation, gap, and overhang of the slat and of the flap whose settings are centered about the values in practice for takeoff. Good agreement with experiments is obtained for prestall angles of attack. Computations show that both C_l and C_l/C_d have an optimum with every design parameter. The trends in the high-lift flow observed are in accordance with both experiments and computations reported in the literature. C_l and C_l/C_d are found to be more sensitive to deviations and gaps than to overhangs.

Nomenclature

C_d	=	drag coefficient
C_l	=	lift coefficient
C_p	=	pressure coefficient
c	=	reference chord (=chord of the retracted configuration in cruise)
G	=	orthogonal gap (normalized with c)
g	=	vertical gap (normalized with c)
M	=	Mach number
O	=	overhang (normalized with c)
Re	=	Reynolds number (based on c)
α	=	angle of attack
α_{stall}	=	stall angle of attack
δ	=	deviation (angle in deg)

Subscripts

f	=	flap
s	=	slat
max	=	maximum
opt	=	optimum
∞	=	free stream

Introduction

AN aircraft's high-lift system may account for approximately 10% of the production cost of a typical jet transport aircraft, and even a 1% increase in $C_{l_{\max}}$ roughly corresponds to an effective increase in the payload of 22 passengers [1]. A thorough understanding of how the slat and flap riggings affect the flow past high-lift systems during takeoff, approach, and landing has tremendous potential. It can help to reduce the wake vortices of an airplane thus enhancing airport capacity. Optimized C_l and C_l/C_d lead to reduced approach altitude and hence increased payload and range. It also can aid improved and simpler designs producing less noise. The present day aircraft industry's need for an efficient, cost-effective design of high-lift systems has caused continued research interest in this subject.

In the past, a wide spectra of topics concerning high-lift systems have been addressed by researchers. Smith's classical paper [2] had already provided far-reaching insight into the physics of high-lift aerodynamics in general, including multielement airfoils, and laid the foundation for subsequent research in this discipline. In the late 1980s, codes coupling the boundary-layer and inviscid solutions were used to compute the flow past multielement airfoils [3,4]. To model the whole gamut of flow phenomena involved, during the early 1990s, the Navier–Stokes equations were solved using algebraic turbulence models [5–9]. It was subsequently established that the choice of the turbulence model and the grid system is crucial to accurately predict high-lift flows. Simultaneously there was considerable progress in developing advanced turbulence models applicable to complex flow regimes [10–12]. High-lift configuration stood as the state-of-the-art test case to validate these new models. Many authors [6,13–17] addressed the issue of turbulence modeling relevant to high-lift flows. Zingg [18] concluded that the Spalart–Allmaras model is appropriate for attached flows and wakes, typically for takeoff flap settings, whereas Menter's SST model fares well in separated flow regimes, typically for landing flap settings. Unstructured grids were preferred by subsequent researchers for their ease of grid adaptation to improve the accuracy of the solution without incurring the penalties associated with global refinement [17,19,20]. Further investigation addressed the relevance of transition in computing the high-lift flows. The accurate prediction of the maximum lift was shown to depend on the correct placement of the laminar-turbulent transition [6,21]. Rumsey et al. [22] reported that inadequate wake prediction may in part also be attributed to deficiencies in specifying the transition on the generating airfoil element. Starting in the late 1990s until very recently, there has been a growing interest in the optimization of multielement airfoils. Gradient based approaches [23–26], robust evolutionary algorithms [27], and hybrid strategies [28], among other techniques have been applied to the optimization of high-lift aerodynamics and flight performance in general.

The above cited efforts have contributed towards improved simulations of high-lift aerodynamics and a better understanding of the flow physics. Most of the work has been concerned with one particular high-lift geometry, that is, using a fixed setting of high-lift devices. Lin and Dominik [29] conducted a brief experimental parametric investigation in NASA's Langley wind tunnel (LTPT). The optimal slat and flap riggings were observed experimentally for a three-element high-lift design airfoil of NASA Langley Research Center. However, in light of recent progress in computational tools and other aspects of simulating high-lift flows, one could undertake an exhaustive computational parametric study involving all design parameters of the multielement high-lift system. Comprehension of

Received 8 August 2005; revision received 2 December 2005; accepted for publication 2 December 2005.

*Guest Scientist, Department of Mechanics.
†Research Scientist, Department of Mechanics; bramkamp@lufmech.rwth-aachen.de.
‡Research Scientist, Department of Mechanics.
§Professor, Department of Mechanics; ballmann@lufmech.rwth-aachen.de. Member AIAA.

the trends observed whereas varying each of the parameters can systematically lead to a better understanding of the flow past high-lift systems in general. The investigations can stand as a guideline for further experimental parametric studies. In addition, they may also aid researchers involved in optimization problems in putting their results of optimum riggings in aerodynamic perspective. Ascertaining the presence of the optimum setting of riggings if any, with regard to C_l and C_l/C_d, ensures that the optimization algorithms would indeed find the global optimum.

With this background, we systematically investigate the effect of flap and slat riggings on the flow past a three-element airfoil system in this paper. The computational study is carried out on the L1/T2 high-lift configuration of the BAC 3-11/RES/30/21 airfoil, described and experimentally tested by Moir [30]. This configuration is currently investigated within the scope of the Collaborative Research Center SFB 401, RWTH Aachen University, Germany: "Flow Modulation and Fluid-Structure-Interaction at Airplane Wings." Throughout this paper we shall refer to this configuration as the reference configuration, which was introduced for takeoff studies and has been the subject of numerical investigation by many researchers in the past [21,22,31–33]. This paper is organized as follows: First, we provide an overview of the computational method and grid generation. Next we outline the validation of the computational tool for the flow past the reference configuration. In the subsequent sections we present the results of the parametric study.

Geometry and Grid Topology

The reference configuration in its experimental setting [30] for takeoff has the following individual element riggings: slat deviation $\delta_s = 25$ deg, flap deviation $\delta_f = 20$ deg, slat gap $g_s = 0.02$, flap gap $g_f = 0.023$, slat overhang $O_s = -0.01$, and flap overhang $O_f = 0$. Two different ways of defining the gaps are reported in the literature, namely, an orthogonal and a vertical definition; see the schematic view in Fig. 1. Note that in the reference configuration the gaps are defined in a vertical sense [30]. However in the parametric study we adopt an orthogonal definition, because it is commonly found in the literature. The slat and flap deviations as well as the angle of attack are measured relative to the axis of the main element, which coincides with the axis of the retracted configuration in cruise.

The computational grid for the reference configuration was provided by DLR, German Aerospace Center, Braunschweig [33]. It is the reference grid for the subsequent parametric study as well. This multiblock structured grid consists of 176,960 cells spread over 8 blocks, with an outer *C* block encompassing several inner blocks. It extends 20 chord lengths both upstream and downstream from the leading edge of the main element and above and below the axis of the main element. The chord length $c = 1.0$ is based on the retracted configuration in cruise. Details of the grid around the reference configuration are shown in Fig. 2. The mesh accounts for various grid

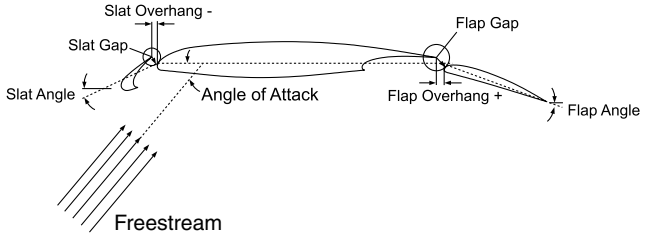

a) Orthogonal definition: G_s= 0.021, G_f= 0.028.

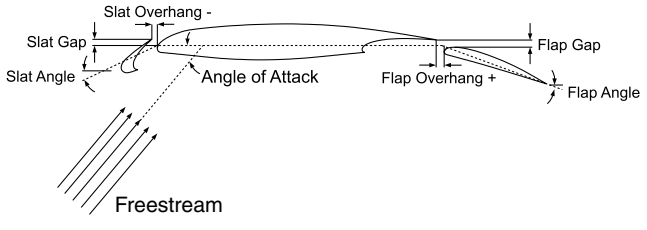

b) Vertical definition: g_s= 0.02, g_f= 0.023

Fig. 1 Geometry of the three-element airfoil system: $\delta_s = 25$ deg, $\delta_f = 20$ deg, $O_s = -0.01$, and $O_f = 0$.

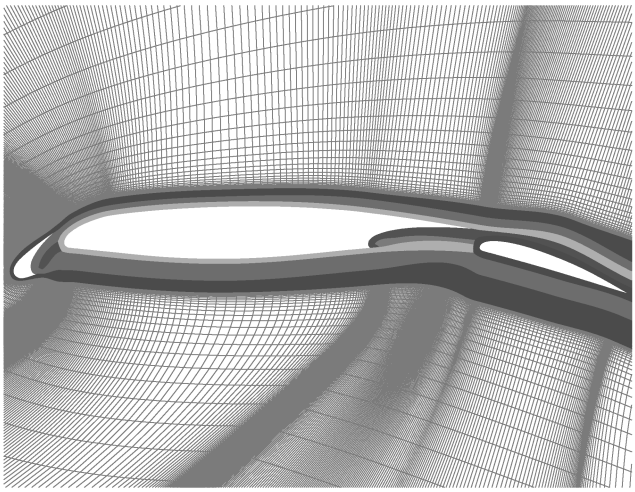

a) The complete grid

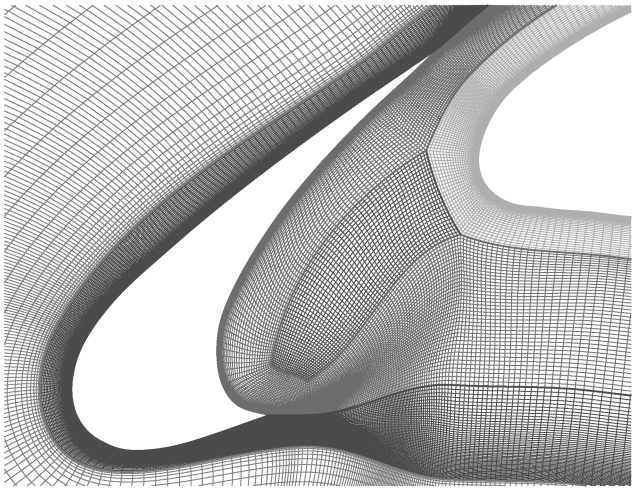

b) The grid around the slat slot

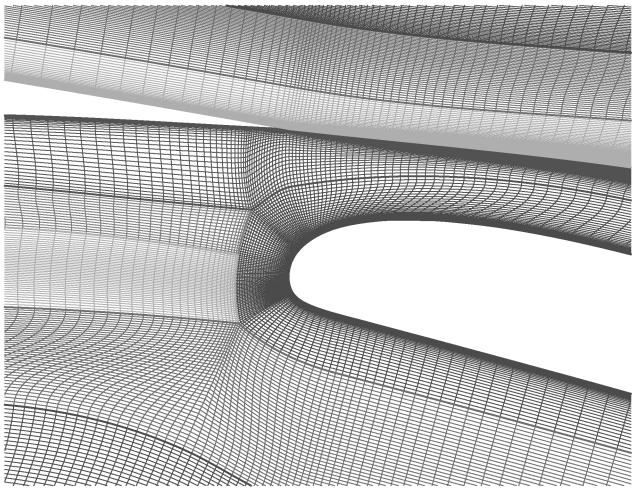

c) The grid around the flap slot

Fig. 2 The reference grid: grid over the reference configuration, $\delta_s = 25$ deg, $\delta_f = 20$ deg, $G_s = 0.021$, $G_f = 0.028$, $O_s = -0.01$, and $O_f = 0$.

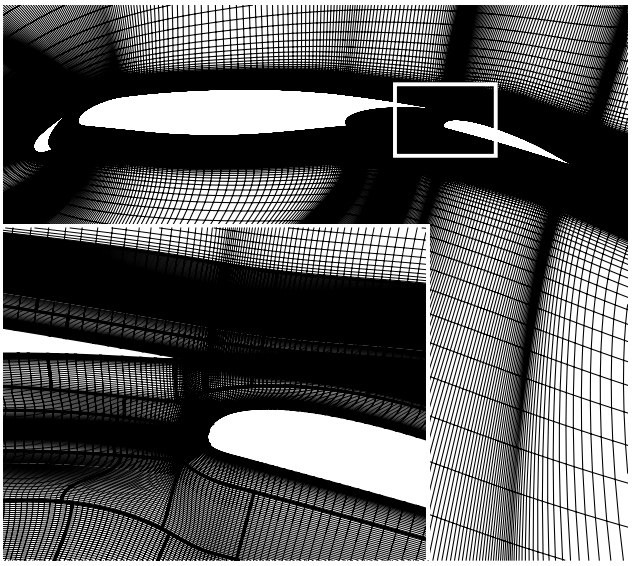

a) Reference configuration, $\delta_f = 20$ deg

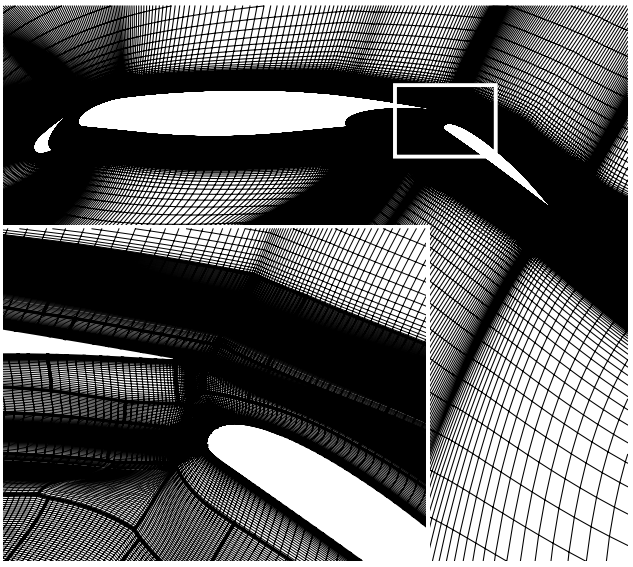

b) Configuration with deflected flap, $\delta_f = 40$ deg

Fig. 3 Deformation of the grid in case of flap deflection. Bold lines: fictitious beam framework.

resolution issues which are crucial to accurately compute the high-lift flow [6]. The inner blocks encompassing the individual elements are highly refined to resolve the propagation of the wakes spreading from the forward elements and flowing over and aft of the successive elements. The streamwise spacing of the grid remains almost constant well aft of the flap, which is found to be necessary to resolve the main-element wake [6]. The normal grid spacing at no-slip walls is about 5×10^{-6}. In the original geometry, that has been tested in the experiments [30], each element of the airfoil system has a blunt trailing edge of finite thickness. To simplify the grid generation all trailing edges were closed [33]. These modifications seem to slightly affect the computed pressure distribution near the trailing edge on the upper surface of the slat.

To define specific slat and flap riggings in the parametric study, the reference grid is conformed to the new configuration of the elements using a new grid deformation algorithm [34], originally proposed for fluid-structure interaction. This approach allows one to generate meshes of high quality for a large number of configurations in a fully automatic way with only little additional user intervention. It models the block boundaries and a certain number of grid lines as elastic beams to form a fictitious beam framework. These beams are considered rigidly fixed together in points of intersection and to surfaces as well, such that the angles are preserved where beams intersect or emerge from a solid surface. This way, the quality of the original mesh can be well preserved even for large deformations, or in the present case for all expected relative displacements and rotations of the different elements of the high-lift configuration. In particular, the orthogonality of the grid near surfaces, the normal wall spacing, and the stretching ratio are well maintained. The deformation of the framework, which is due to displacements of the surface grid nodes, is calculated by a finite-element solver. The new positions of grid points in the interior of the domain which are not included in the beam framework are computed by interpolation. As an example, Fig. 3 shows the original reference configuration and the configuration with deflected flap, respectively. The bold lines in the detailed view represent the fictitious beam framework.

Computational Methodology

In the present study, flow computations are performed using QUADFLOW [35–38], which solves the Reynolds-averaged Navier–Stokes equations for viscous compressible fluid flow. The flow is assumed to be fully turbulent in the numerical simulation. Turbulence is considered by the one-equation model according to Spalart and Allmaras [11]. The spatial discretization of the governing equations is based on a cell centered finite volume scheme suited for unstructured meshes of arbitrary topology. It is of second order in space, employing a linear Green–Gauss reconstruction technique. To account for the directed transport of information, the inviscid fluxes are discretized with the HLLC flux-difference splitting, originally proposed by Harten, Lax, and van Leer, which is also capable to resolve contact waves in the present formulation due to Batten et al. [39] with modified wave speeds according to Davis [40]. Far field boundary conditions are imposed using a circulation correction method [41]. The solution is advanced in time by an implicit Euler method to reach steady state. Its implementation is based on a Newton–Krylov–Schwarz approach. Interfaces to various grid generation systems do exist within QUADFLOW, enabling the use of multiblock structured meshes as well.

Access to a state-of-the-art computing environment and the fabrication of an automated organizational approach, capable of being used in a design environment, eased the inherent complexity of the mass-scale study being undertaken. The sequence of operations, namely, 1) the grid generation for different riggings using the grid deformation algorithm, 2) fluid flow computation, and 3) post-processing of results, were automated using programming and scripting languages. This automation resulted in a robust and reusable tool, which enabled us to perform over 1000 cycles of operations in the present study. Computations were run in parallel mode on the Sun Fire cluster of the computer center at RWTH Aachen University, Germany. It houses 768 dual-core CPU's based on Ultra SPARC 4 processors yielding up to a total of 4.6 TFlops peak performance and 3 TB main memory. Throughout this study, the flow is considered to be sufficiently converged when the residual of the density is decreased by 7 orders of magnitude, based on its initial value. On an average each computation took about 4000 nonlinear iterations to converge, which required about 2 h of CPU time on 20 processors.

Code Validation

In this section we present the comparison between the computed and experimental results for the reference configuration. The flow was simulated at $M_\infty = 0.197$, $Re = 3.52 \times 10^6$ and two different angles of attack $\alpha = 4.01$ deg, 20.18 deg, for which experimental data are available in the literature [30]. These measurements are known for their accuracy due to the high degree of two dimensionality of the flowfield in the wind tunnel. The flow is assumed to be fully turbulent in the numerical simulation. Figure 4 shows the comparison between the predicted surface pressure coefficient with experimental data at $\alpha = 4.01$ deg and $\alpha = 20.18$ deg, respectively. Overall, good agreement is obtained

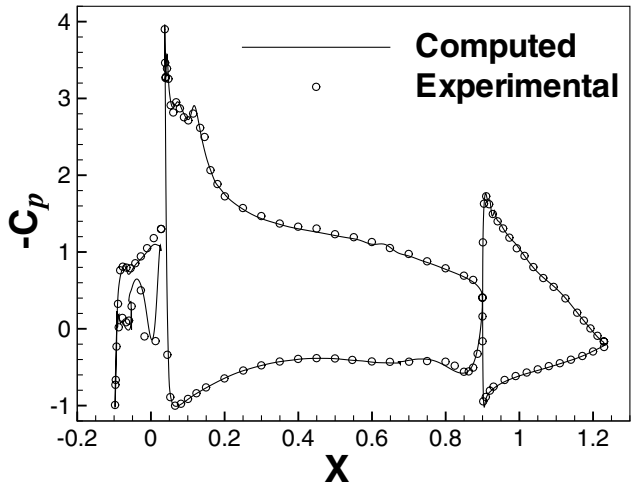

a) Cp at α= 4.01 deg

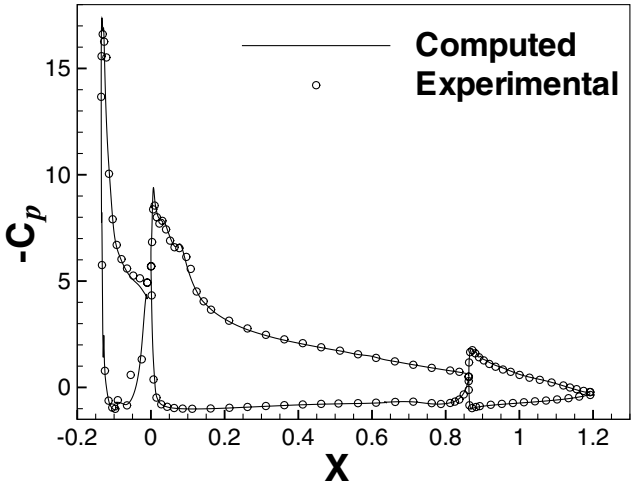

b) Cp at α = 20.18 deg

Fig. 4 Computed and experimental Cp distribution: $\delta_s = 25$ deg, $\delta_f = 20$ deg, $G_s = 0.021$, $G_f = 0.028$, $O_s = -0.01$, $O_f = 0$, $M_\infty = 0.197$, and $Re = 3.52 \times 10^6$.

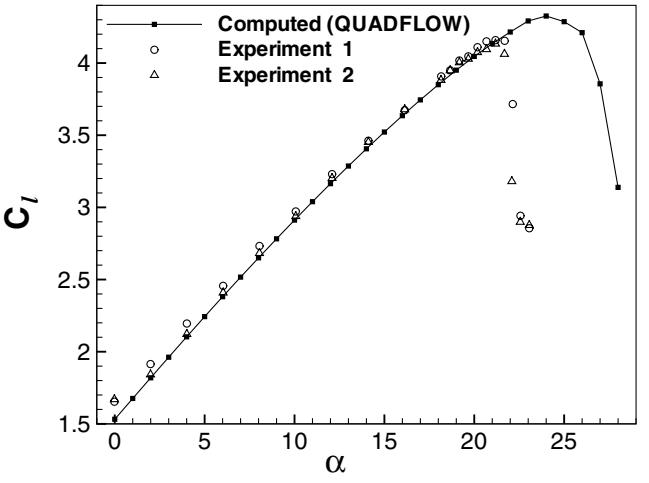

a) C_l vs α

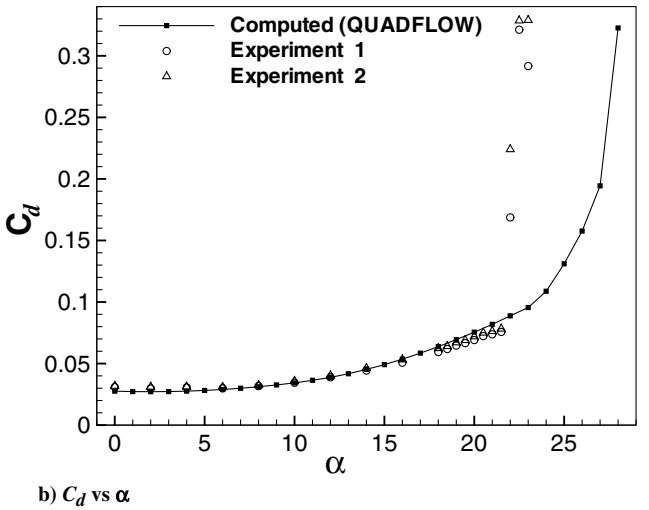

b) C_d vs α

Fig. 5 Computed and experimental load coefficients: $\delta_s = 25$ deg, $\delta_f = 20$ deg, $G_s = 0.021$, $G_f = 0.028$, $O_s = -0.01$, $O_f = 0$, $M_\infty = 0.197$, and $Re = 3.52 \times 10^6$.

even at a higher angle of attack. At the trailing edge of the slat, the pressure distribution is slightly underpredicted. We believe that this is primarily due to the fact that the experimental model has blunt trailing edges whereas they are closed in the computational grid; see the section on "Geometry and Grid Topology." On the upper surfaces of the main element and the flap, near their leading edges, oscillations in the pressure are predicted. In our experience, this is caused by surface waviness, as also noted by Fejtek [32].

Figure 5 shows the comparison of the computed and experimental C_l and C_d as a function of the angle of attack. The experimental data correspond to two repeated sets of wind tunnel runs carried out [30] and have been corrected for the wind tunnel wall effects. Lift and drag agreement is good in the intermediate range of the angle of attack, $4 \leq \alpha \leq 18$ deg. In comparison with the experiments, the lift is underpredicted by the computations. This trend has also been observed by other researchers in their numerical results [21,22,32]. Near the experimental stall angle, lift is less than 3% underpredicted and drag is about 4% overpredicted. At lower angles of attack ($\alpha < 2$ deg), lift is nearly 10% underpredicted. Stall is predicted at $\alpha_{\text{stall}} \approx 24$ deg, which is about 3 deg higher than the experimental stall angle. The qualitative stall type predicted by the computations is that of a trailing edge type (characterized by a gradual rounding over of the lift curve at $C_{l_{\max}}$) whereas the experiments show a leading edge-type stall (characterized by an abrupt loss in lift after stall). Concerning the maximum lift, computations yielded $C_{l_{\max}} = 4.32$ at $\alpha = 24$ deg although the experiments show $C_{l_{\max}} = 4.16$ at $\alpha = 21.18$ deg. This amounts to an overprediction of $C_{l,\max}$ by about 4%. A similar overprediction was also observed by other researchers [6,20]. It is interesting to note that the computed $C_{l_{\max}} = 4.32$ matches with that predicted by CFL3D from NASA Langley (an implicit upwind finite volume method employing Roe flux-difference splitting and the Spalart–Allmaras turbulence model) [32]. Nelson [21] found that the correct placement of the laminar-turbulent transition on the slat is essential to accurately predict maximum lift. By locating the transition point just aft of the laminar separation, thus causing reattachment, Nelson [21] was able obtain an accurate prediction of maximum lift. The general disagreement in lift and drag at lower and near-stall angles of attack can be attributed, among others, to the probable 3-D effects in the nature of experiments inside the wind tunnel [20,42] and to the lack of boundary-layer transition in the flow simulation [5,6,22,29].

Figure 6a shows the development of the flowfield for $\alpha = 18$, 21, 24, and 28 deg. As α is increased, the flow hitting the leading edge of the slat drifts to the right. This gradual change in course affects the thickness of the slat cove vortex, which achieves its minimum at $\alpha = 24$ deg. At the same time, the average speed of the flow through the slat slot reaches its maximum value. Figure 6b shows that as α is increased, initially one can observe the following features: 1) the wake of the slat gradually grows even whereas the flow over the slat is attached, 2) the main-element wake convected over the flap is seen to spread rapidly aft of it through the adverse pressure gradient zone, 3) the interaction between the wakes of the slat and the main element is strengthened, aft of the flap, and 4) minor flow separation is

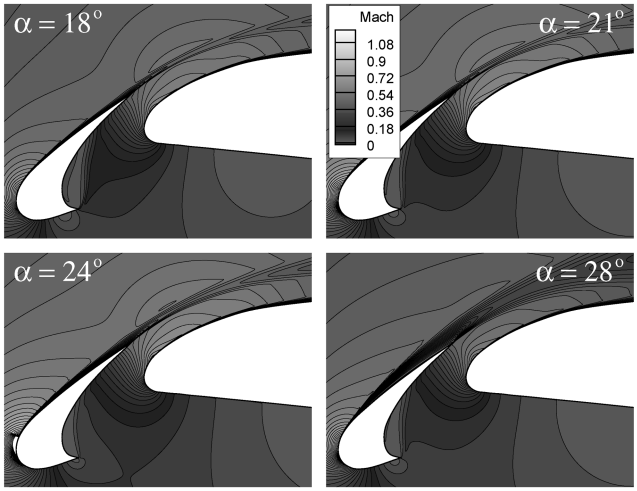

a) Mach contours through the slat slot

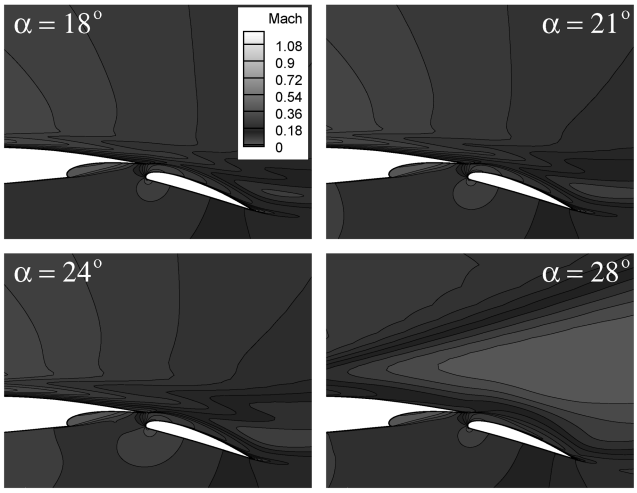

b) Mach contours through the flap slot

Fig. 6 Mach contours at different α: $\delta_s = 25$ deg, $\delta_f = 20$ deg, $G_s = 0.021$, $G_f = 0.028$, $O_s = -0.01$, $O_f = 0$, $M_\infty = 0.197$, and $Re = 3.52 \times 10^6$.

observed over the flap near its trailing edge. At $\alpha = 24$ deg, for which the computation predicts stall, the sonic flow above the leading edge of the slat creates a tremendous slat suction as shown in Fig. 7. Its downwash increases the main-element suction as well. The shock-induced laminar separation on the slat is seen to effect stall on the present configuration, consistent with Nelson [21]. As the angle of attack is increased beyond α_{stall}, the shock interacts with the boundary layer which leads to flow separation above the slat, near its trailing edge. For $\alpha \geq \alpha_{\text{stall}}$, the separated boundary layer over the slat causes its wake to considerably grow in thickness. The thickened wake moves over the successive elements decelerating the flow en route, which reduces the loading. Furthermore it leads to an off-body separation over the entire main element and the flap, as shown in Fig. 6b for $\alpha = 28$ deg. As a result, the pressure all over the upper surface of the main element as well as the pressure peak of the flap is significantly reduced; see Fig. 7. Beyond the computed stall angle, the wake of the main element confines the jet through the flap slot to a narrow layer above the upper surface of the flap. As a result, the flap boundary layer reattaches near its trailing edge, which is characteristic for high-lift flows at higher angles of attack [6]. It leads a small gain in lift over the rear part of the flap's upper surface.

Parametric Study

In this section we investigate the effect of flap and slat riggings on the 2-D high-lift flow. We confine our study to angles of attack

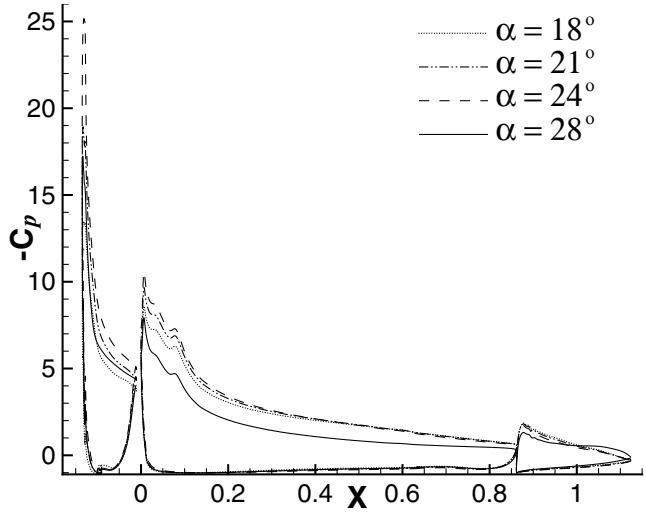

Fig. 7 Cp distribution at prestall, stall, and poststall angles of attack: $\delta_s = 25$, $\delta_f = 20$ deg, $G_s = 0.021$, $G_f = 0.028$, $O_s = -0.01$, $O_f = 0$, $M_\infty = 0.197$, and $Re = 3.52 \times 10^6$.

$\alpha \leq 16$ deg, for which a good and reliable agreement with experiments was reported for the reference configuration in the previous section. We begin by varying the gap, overhang, and deviation of the slat whereas the flap riggings are set according to the reference configuration: $\delta_f = 20$ deg, $G_f = 0.028$, and $O_f = 0$. The emerging trends always show the presence of an optimum C_l and C_l/C_d. Next the gaps, overhangs, and deviations of the flap are varied by positioning the slat riggings at their optimal values.

Effect of Slat Riggings

In the following, the effects of slat riggings are investigated, whereas the flap riggings remain unchanged according to the reference configuration settings: $\delta_f = 20$ deg, $G_f = 0.028$, and $O_f = 0$. The slat gap and the slat overhang are varied for four different slat deviations: $\delta_s = 15$, 20, 25, and 30 deg. Later, the slat deviations are varied whereas gaps and overhangs are set to their optimal values. For brevity, only the results for $\alpha = 12$ deg are reported.

First we investigate the effect of the slat gap (G_s). Figure 8a shows the variation of C_l with a slat gap for different δ_s. For all slat deviations deployed, the lift is found to have a maximum amidst the range of slat gaps studied. The variation of C_l/C_d is shown in Fig. 8b. C_l/C_d achieves its maximum nearly at the same value of slat gaps as C_l. As δ_s is increased, both C_l and C_l/C_d reach their optima at smaller slat gaps. The variations of C_l and C_l/C_d are found to be qualitatively similar at different α. To have a qualitative look at the change of the flowfield with increasing slat gap, we examine the flow for a typical lower slat setting at $\delta_s = 15$ deg and $\alpha = 12$ deg. In Fig. 9, observe that as G_s is increased the slat moves vertically away from the leading edge of the main element such that the slat overhang remains constant. In this particular case with $\delta_s = 15$ deg and $\alpha = 12$ deg, the flow from the freestream is almost in line with the axis of the slat. Hence, the flow can directly rush through the slat slot, as shown in Fig. 9a, where six streamlines all originating at fixed locations far upstream in the domain are depicted. As a result when the slat gap becomes larger there is an increased volume of accelerated flow through the slat slot. When the freestream flow is not in line with the axis of the slat, it cannot rush through the slat slot without hindrance. Hence, the lift and the lift to drag ratio achieve their optima at different slat riggings. Figure 9b shows the distribution of the Mach number around the slat. As the slat gap is increased, the Mach number below the slat and through the slat slot increases in general. As a result, the pressure decreases along the slat cove as well as on the lower surface of the main element underneath its leading edge; see Fig. 10. As G_s is increased the flow around the upper surface of the slat is slowed down causing the slat's suction peak to drop. However, the suction peak over the main element

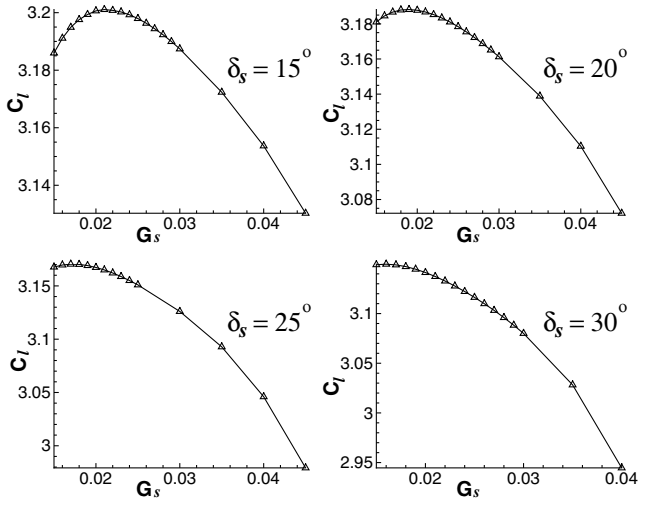

a) C_l vs slat gap

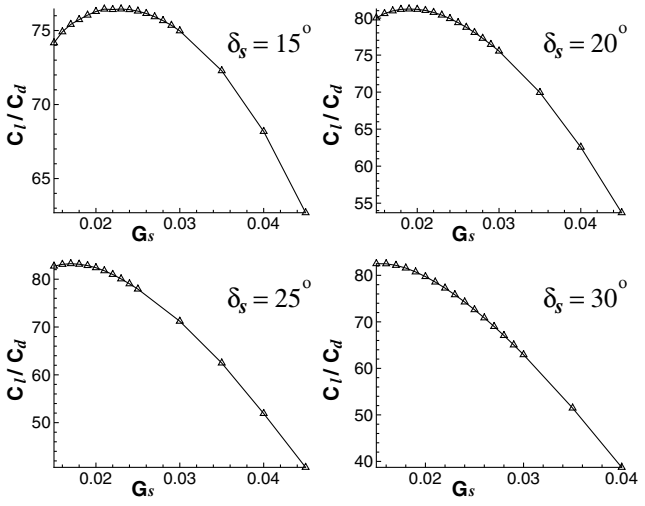

b) C_l/C_d vs slat gap.

Fig. 8 Load coefficients as a function of the slat gap at various slat deviations: $\delta_f = 20$ deg, $G_f = 0.028$, $O_s = -0.01$, $O_f = 0$, $\alpha = 12$ deg, $M_\infty = 0.197$, and $Re = 3.52 \times 10^6$.

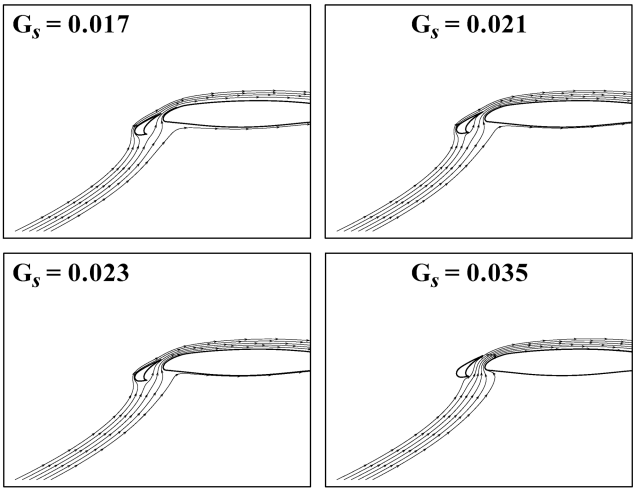

a) Far-field streamlines gushing through the slat slot

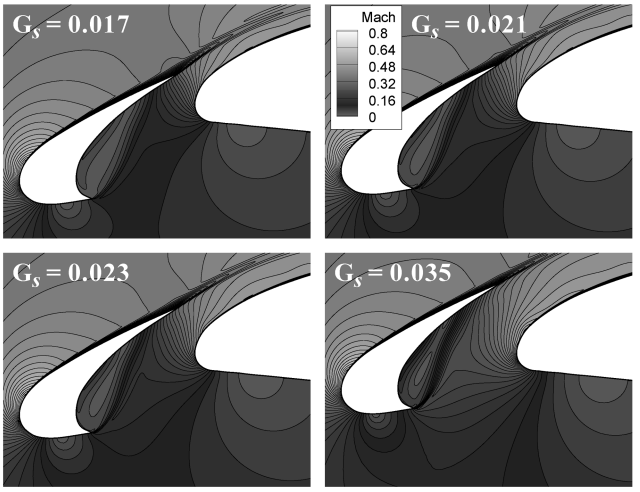

b) Mach contours through the slat slot

Fig. 9 Mach contours at different slat gaps: $O_s = -0.01$, $O_f = 0$, $\delta_s = 15$ deg, $\delta_f = 20$ deg, $G_f = 0.028$, $\alpha = 12$ deg, $M_\infty = 0.197$, and $Re = 3.52 \times 10^6$.

grows as G_s is increased, thus enhancing the lift. In addition the lift is gradually enhanced above the upper surface of the slat near its trailing edge. The interplay between these lift-enhancing and lift-reducing factors leads to $C_{l_{\text{opt}}} = 3.201$ at $G_s = 0.021$, $\delta_s = 15$ deg. On the other hand $(C_l/C_d)_{\text{opt}} = 83.2$ is achieved at a lesser gap $G_s = 0.017$, $\delta_s = 25$ deg. For gaps larger than $G_{s_{\text{opt}}}$, losses in the lift are incurred all along the slat cove; see Fig. 10. These losses are larger in magnitude than the gains due to the main element, driving the cumulative lift over the three-element system down. Because changing the slat gap has a negligible effect aft of the main element, we have not shown the details in that region.

Next we study the effect of slat overhang (O_s). Four slat deviations: $\delta_s = 15$, 20, 25, and 30 deg are considered while positioning the slat gaps at their corresponding optima; see Table 1. Figure 11a shows the variation of C_l with slat overhang. For all slat deviations considered, the lift is found to have a maximum amidst the range of slat overhangs studied. C_l/C_d as a function of O_s for different δ_s is shown in Fig. 11b. Again C_l/C_d and C_l achieve their maxima nearly at the same values of slat overhangs. The maximum is shifted towards smaller overhangs as δ_s is increased. A qualitative study of the flowfield is shown for different slat overhangs in Fig. 12, with $\delta_s = 20$ deg, $\alpha = 12$ deg and optimum gap $G_{s_{\text{opt}}} = 0.019$. The orthogonal gap is kept constant by maintaining the shortest distance

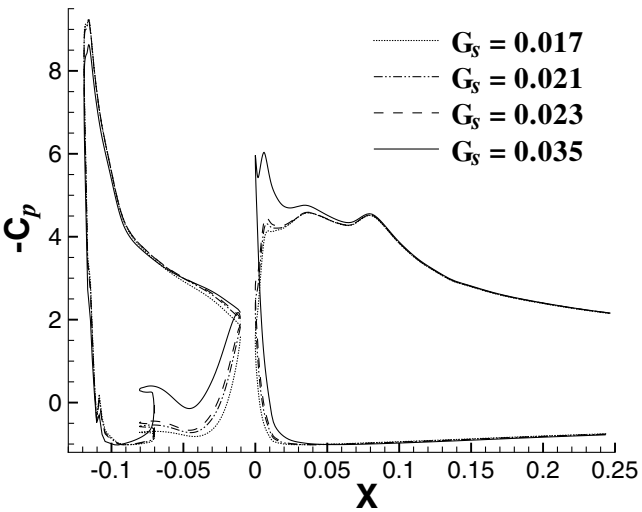

Fig. 10 C_p distribution over the slat and the main element at different G_s: $O_s = -0.01$, $O_f = 0$, $\delta_s = 15$ deg, $\delta_f = 20$ deg, $G_f = 0.028$, $\alpha = 12$ deg, $M_\infty = 0.197$, and $Re = 3.52 \times 10^6$.

Table 1 Optimum slat gaps

δ_s	$G_{s_{\text{opt}}}$	$C_{l_{\text{opt}}}$	$(C_l/C_d)_{\text{opt}}$
15 deg	2.1%	3.20	76.5
20 deg	1.9%	3.19	81.2
25 deg	1.7%	3.17	83.2
30 deg	1.6%	3.15	82.5

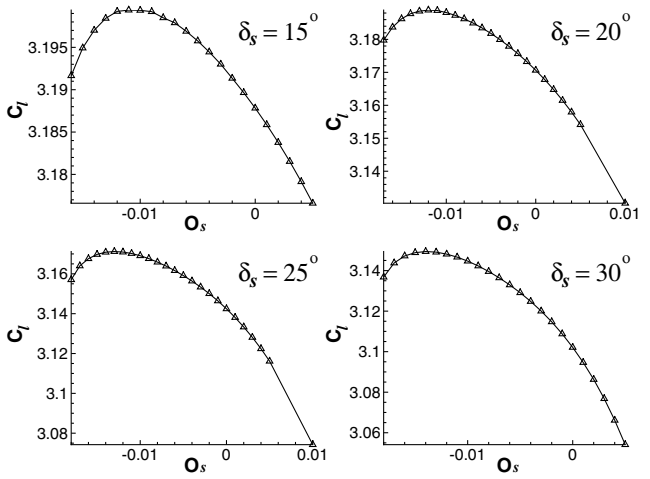

a) C_l vs slat overhang (at $G_{s_{opt}}$)

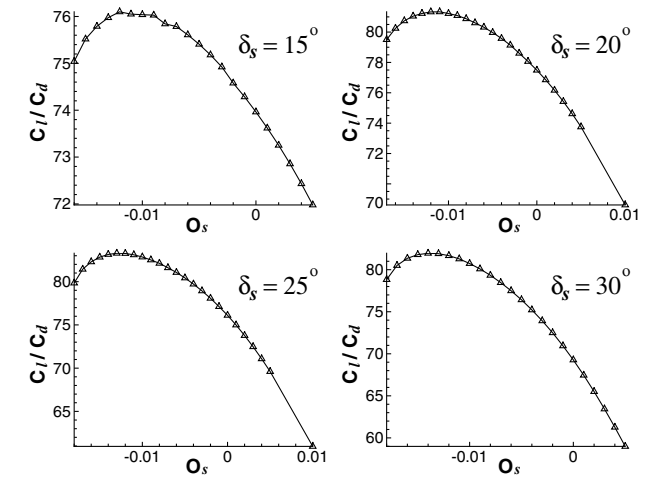

b) C_l/C_d vs slat overhang (at $G_{s_{opt}}$)

Fig. 11 Load coefficients as a function of the slat overhang at various slat deviations: $\delta_f = 20$ deg, $G_f = 0.028$, $O_f = 0$, $\alpha = 12$ deg, $M_\infty = 0.197$, and $Re = 3.52 \times 10^6$.

between the trailing edge of the slat and the main-element surface equal to $G_{s_{\text{opt}}}$. As the slat overhang is increased, the slat element slides upward over the leading edge of the main element toward it. For $\delta_s = 20$ deg, $\alpha = 12$ deg, the freestream flow is more deviated from the axis of the slat than it was in the case before, when we varied the slat gap. Hence one can observe lower Mach numbers in general due to the obstruction rendered by the increased slat deviation ($\delta_s = 20$ deg as opposed to $\delta_s = 15$ deg before). Figure 12a shows selected far-field streamlines. As the overhang is increased, the geometry of the passage between the slat and the main element changes in such a way that the flow through the slat slot is further accelerated. At larger O_s, the flow hits the lower surface of the slat at a point increasingly away from its trailing edge, such that the extent of the slat cove vortex is decreased. As the overhang is increased, the upwash due to the accelerated jet through the slat slot causes higher suction over the upper surface of the slat; see Fig. 13. However the suction peak of the main element drops as O_s is increased. This is

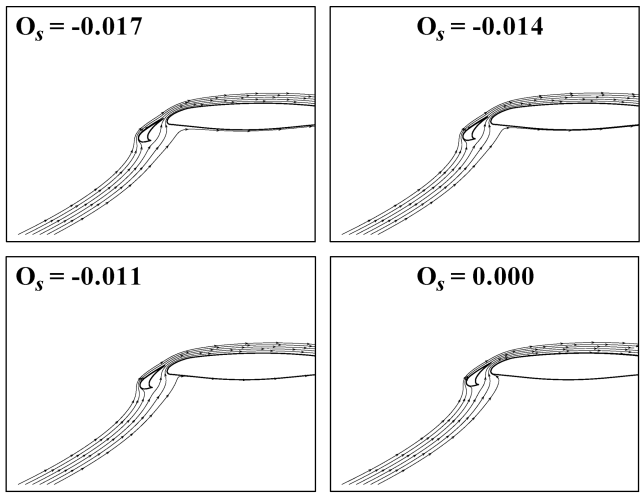

a) Far-field streamlines gushing through the slat slot

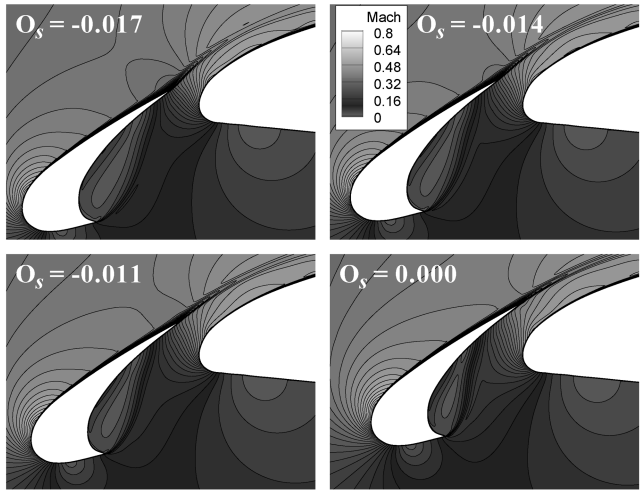

b) Mach contours through the slat slot (at $G_{s_{opt}}$)

Fig. 12 Mach contours at different slat overhangs: $\delta_s = 20$ deg, $\delta_f = 20$ deg, $G_s = 0.019$, $G_f = 0.028$, $O_f = 0$, $\alpha = 12$ deg, $M_\infty = 0.197$, and $Re = 3.52 \times 10^6$.

because the slat is now placed above the main element and impedes the jet speeding from down under. The greater the positive overhang, the more the slat blocks the jet and slows down the flow above the upper surface of the main element near its leading edge. As O_s is increased, initially the slat element enhances the lift whereas the main element incurs losses. At $O_s = -0.011$ and $\delta_s = 15$ deg, the lift achieves $C_{l_{\text{opt}}} = 3.199$. Beyond that, the slat starts to incur significant losses in the cove region causing the cumulative lift over the three-element system to drop. One observes a negligible effect on the flowfield aft of the main element by changing the slat overhang.

Finally we study the effect of slat deviation (δ_s). The computed lift decreases monotonically as the slat deviation is increased (in a nose-down sense) for the entire range of slat gaps and overhangs. This behavior of the lift is expected because the slat is a forward element. At lower and moderate G_s and α, C_l/C_d also decreases monotonically. However, at larger gaps and angles of attack, there exist C_l/C_d optima. As an example, we present the results for $G_s = 0.025$. Figure 14 shows the variation of C_l and C_l/C_d with δ_s for three different angles of attack: $\alpha = 0.00$, 4.01, and 12.00 deg. The lift decreases gradually all along, whereas C_l/C_d varies faster, that is, the drag changes faster than the lift. Figure 15a shows the distribution of the Mach number around the slat for $\alpha = 12$ deg and four different values of δ_s. As δ_s is increased, mainly two opposing factors seem to influence the lift: the flow above the upper surface of the slat is decelerated, whereas it is accelerated through the slat slot. Both effects lead to a reduction in lift generated by the slat. On the

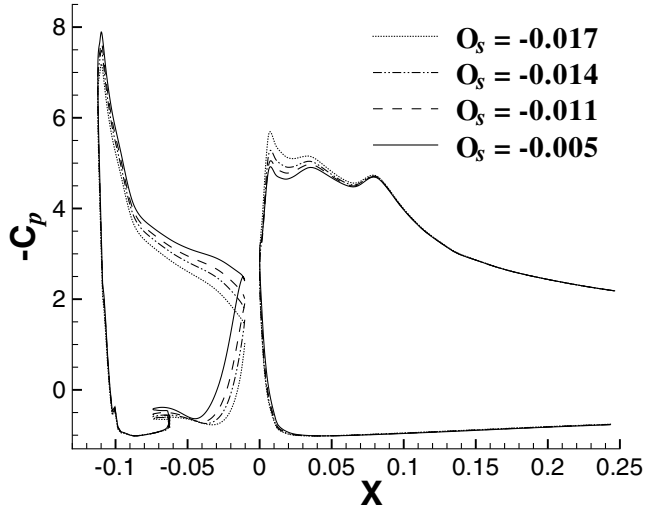

Fig. 13 C_p distribution over the slat and the main element at different O_s: $\delta_s = 20$ deg, $\delta_f = 20$ deg, $G_s = 0.019$, $G_f = 0.028$, $O_f = 0$, $\alpha = 12$ deg, $M_\infty = 0.197$, and $Re = 3.52 \times 10^6$.

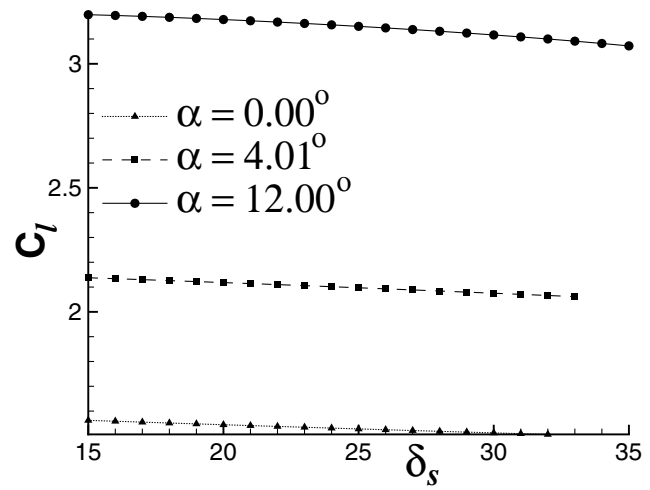

a) C_l vs slat deviation

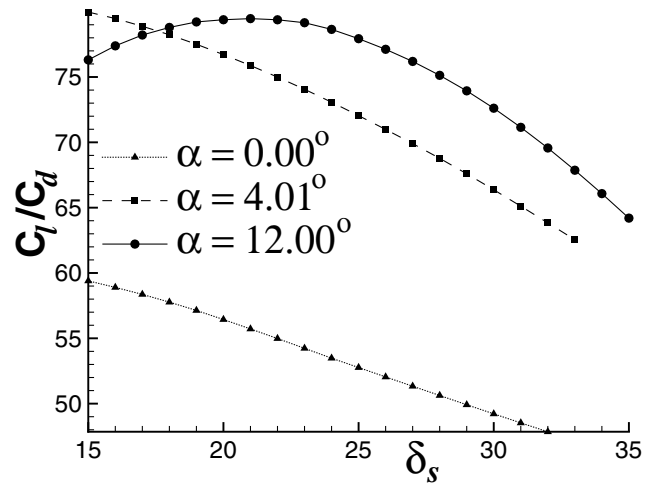

b) C_l/C_d vs slat deviation

Fig. 14 Load coefficients as a function of the slat deviation at various α: $G_s = 0.025$, $O_s = -0.01$, $\delta_f = 20$ deg, $G_f = 0.028$, $O_f = 0$, $M_\infty = 0.197$, and $Re = 3.52 \times 10^6$.

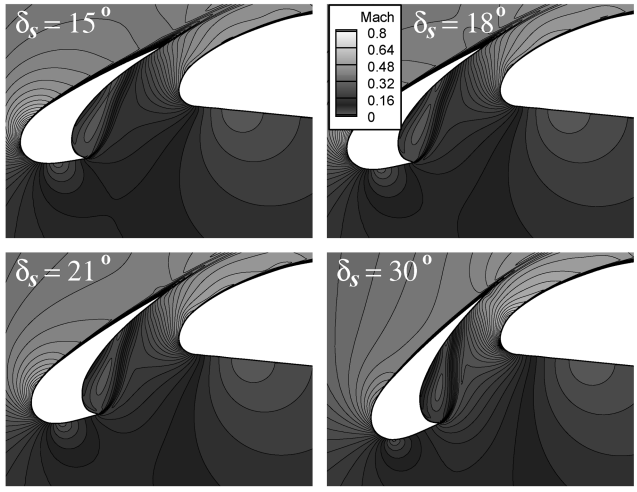

a) Mach contours through the slat slot

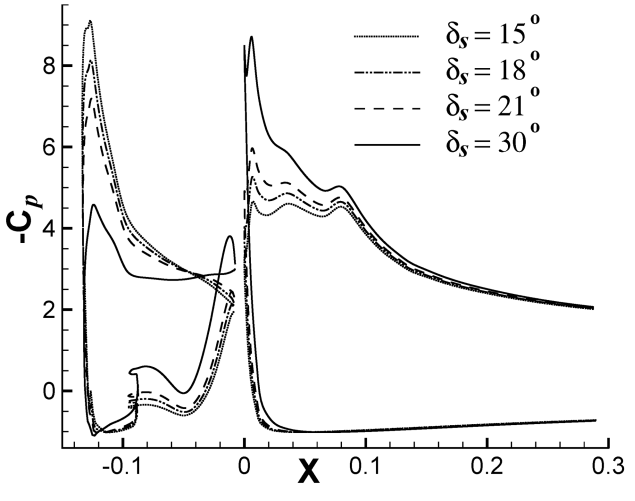

b) C_p Over the slat and main element

Fig. 15 Development of the flow with δ_s: $G_s = 0.025$, $O_s = -0.01$, $\delta_f = 20$ deg, $G_f = 0.028$, $O_f = 0$, $\alpha = 12$ deg, $M_\infty = 0.197$, and $Re = 3.52 \times 10^6$.

other hand there is a significant gain in the suction peak of the main element.

The qualitative trends observed in the computed results presented above are consistent with the trends reported in the experimental study on NASA's Langley high-lift airfoils [29]. The effect of increasing slat riggings in general is seen to affect the slat's circulation drastically. At higher deployment of each of the slat parameters, losses incurred under the slat cove are predominant which reduce the cumulative lift. However, for small and moderate deployments of the slat parameters, a contrasting effect on the loading of the slat and of the main element can be observed. Changing the slat gap primarily influences the main-element loading and secondarily the slat loading, as also reported in [29]. Changing slat overhang results in nearly balanced changes in loading on both the slat and the main element, but losses under the cove play the decisive role at higher riggings. Changing the slat deviation predominantly reduces the suction peak on the slat, which is consistent with observations made by Lin and Dominik [29]. It is always the relative orientation of the elements which influence the load coefficients and the aerodynamic performance in general. The angle of attack and the slat deviation act to direct the flow along or deviate it off the axis of the slat which primarily affects the slat suction. The gap and the overhang determine the extent of the intervening space between the slat and the main element, thus affecting the main-element suction and the cove vortex of the slat. In the present study, at late takeoff $\alpha = 12$ deg, C_l/C_d achieves its

Table 2 Optimum slat overhangs at $G_{s_{opt}}$

δ_s	$O_{s_{opt}}$	$C_{l_{opt}}$	$(C_l/C_d)_{opt}$
15 deg	−1.1%	3.20	76.1
20 deg	−1.2%	3.19	81.3
25 deg	−1.3%	3.17	83.3
30 deg	−1.4%	3.15	82.0

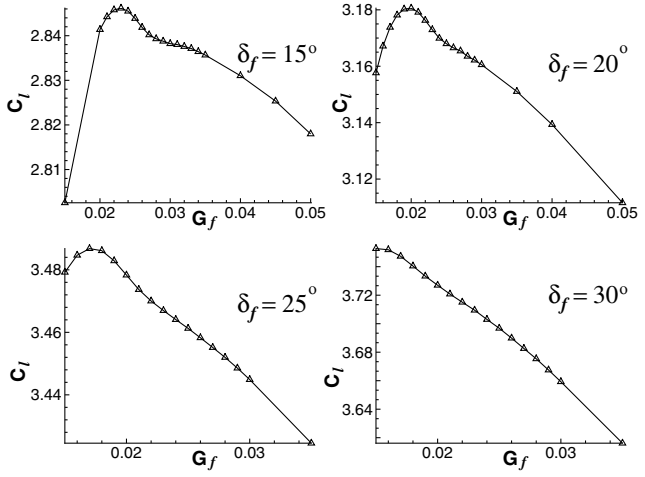

a) C_l as a function of the flap gap.

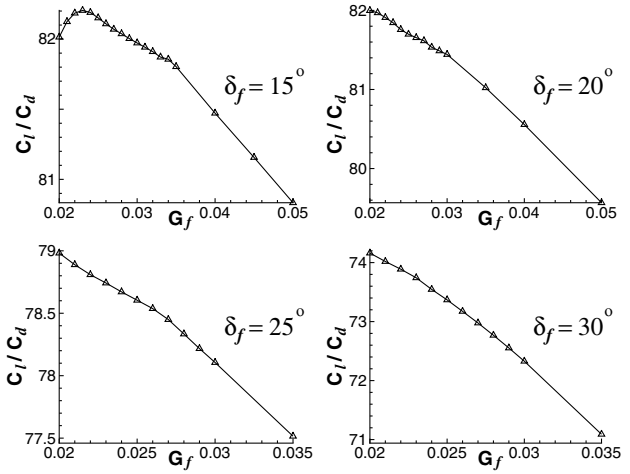

b) C_l/C_d as a function of the flap gap

Fig. 16 Load coefficients as a function of the flap gap at various flap deviations: $O_f = 0, \delta_s = 25$ deg, $G_s = 0.021, O_s = -0.01, M_\infty = 0.197$, and $Re = 3.52 \times 10^6$.

maximum at $\delta_s = 25$ deg; see Figs. 8 and 11 and Tables 1 and 2. At this slat deviation, $C_l = 3.17$ and $(C_l/C_d)_{opt} = 83.3$ are achieved at $G_s = 0.017$ (vertical gap $g_s = 0.013$) and $O_s = -0.013$. Note that the slat riggings of the reference configuration ($G_s = 0.021$, $O_s = -0.01$, and $\delta_s = 25$ deg) are close to these optimal settings.

Effect of Flap Riggings

In this parametric study concerning the flap riggings we choose the slat riggings according to the reference configuration ($\delta_s = 25$ deg, $G_s = 0.021$, and $O_s = -0.01$). In the previous section we observed that the optimal slat riggings are centered about the settings of the reference configuration. Typical flap deviations for takeoff and landing are $\delta_f = 20$, 30 deg, respectively. For brevity, only the results for $\alpha = 12$ deg are reported.

First the effect of the flap gap (G_f) is investigated. Figure 16a shows C_l as a function of G_f at $\alpha = 12$ deg for four different flap

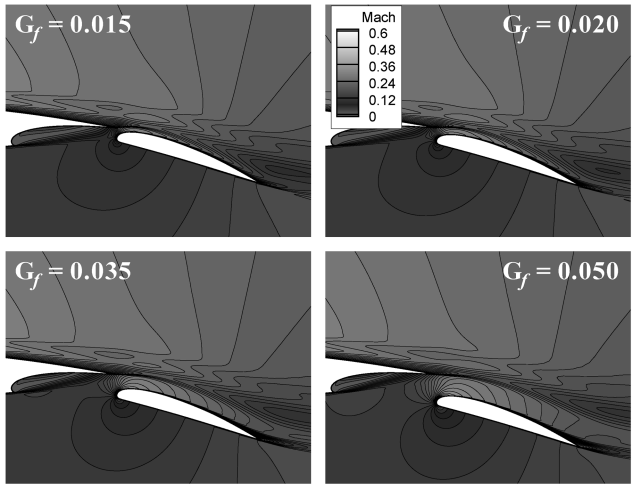

a) Mach contours through the flap slot at different G_f

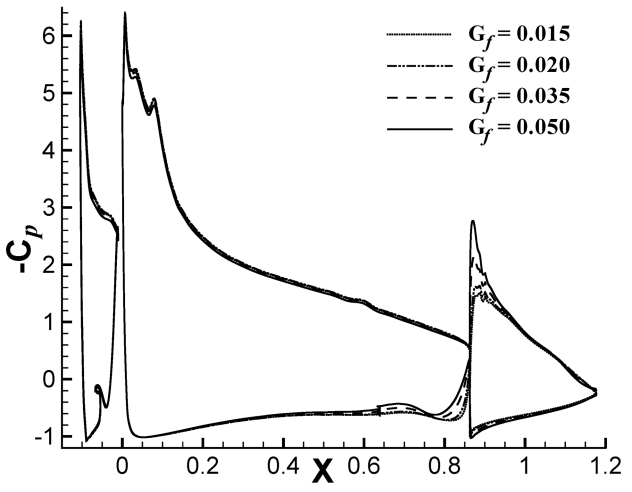

b) C_p at different G_f

Fig. 17 Development of the flow through the flap slot: $O_f = 0$, $\delta_f = 20$ deg, $\delta_s = 25$ deg, $G_s = 0.021$, $O_s = -0.01$, $\alpha = 12.00$ deg, $M_\infty = 0.197$, and $Re = 3.52 \times 10^6$.

deviations: $\delta_s = 15$, 20, 25, and 30 deg. For each flap deviation considered, the lift is found to have an optimum. Similar trends are observed for C_l/C_d; see Fig. 16b. Figure 17a shows the distribution of the Mach number around the flap for different G_f at $\delta_f = 20$ deg and $\alpha = 12$ deg. As the flap gap is increased, an increased volume of air rushes through the widening passage underneath the trailing edge of the main element. One can observe a general increase in the Mach number within the main-element cove region and through the flap slot. The accelerated flow in the passage is found to have opposing effects on the flap and the main-element cove: the flap suction peak increases whereas the pressure in the cove of the main element decreases, as depicted in Fig. 17b. The interplay between these opposing effects leads to $C_{l_{opt}} = 3.75$ (at $G_f = 0.015$, $\delta_f = 30$ deg) whereas $(C_l/C_d)_{opt} = 82.0$ (at $G_f = 0.020$, $\delta_f = 20$ deg); see Table 3. For $G_f < 0.023$, there is a strong interaction between the wake spreading from the main element with the flap boundary layer. There is only a very small flow separation on the upper surface of the flap, near its trailing edge. Beyond $G_{f_{opt}}$, the wakes drift away from the flap boundary layer which leads to increased flow separation near the trailing edge of the flap. As a result, minor losses in lift over the flap's upper surface near its trailing edge are seen in the corresponding C_p distribution; see Fig. 17b. Further note that for lower values of the flap gap, changing the setting of the flap gap has only a weak influence on the main element and on the slat. At higher G_f, the upwash of the accelerated flow through the flap slot reduces the loading on both the main element and the slat. Thus, the

Table 3 Optimum flap gaps

δ_f	$G_{f_{opt}}$	$C_{l_{opt}}$	$(C_l/C_d)_{opt}$
15 deg	2.3%	2.85	82.2
20 deg	2.0%	3.18	82.0
25 deg	1.7%	3.49	79.2
30 deg	1.5%	3.75	74.9

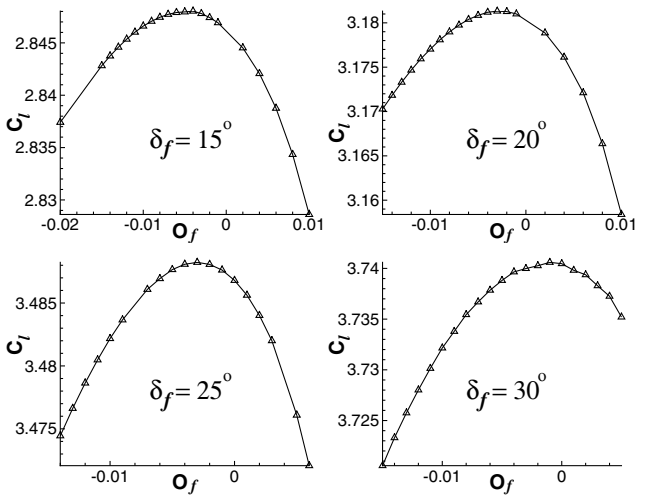

a) C_l as a function of the flap overhang (at $G_{f_{opt}}$)

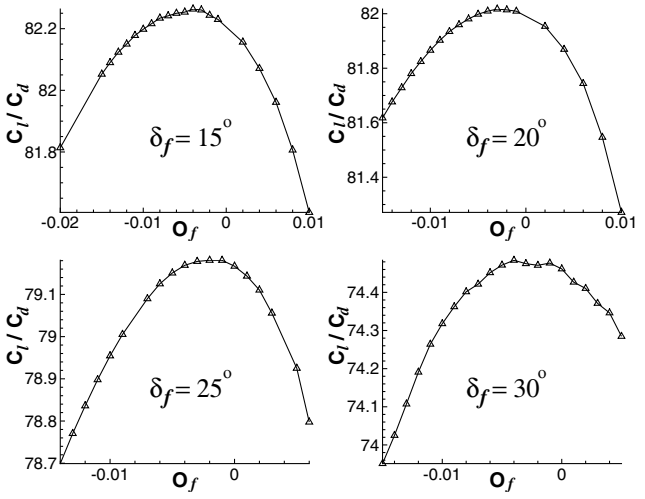

b) C_l/C_d as a function of the flap overhang (at $G_{f_{opt}}$)

Fig. 18 Load coefficients as a function of the flap overhang at various flap deviations: $\delta_s = 25$ deg, $G_s = 0.021$, $O_s = -0.01$, $M_\infty = 0.197$, and $Re = 3.52 \times 10^6$.

cumulative lift of the three-element airfoil system decreases, predominantly driven by the losses incurred by the main element.

Next we study the effect of the flap overhang (O_f). The flap gaps are deployed at their optimal setting for corresponding flap deviations, as determined in the previous section; see Table 3. The orthogonal gap is kept constant by maintaining the shortest distance between the trailing edge of the main element and the flap upper surface. When different overhangs are imparted at constant flap gaps, the flap element moves mainly horizontally underneath the trailing edge of the main element. For positive overhangs the flap moves away from the main element whereas for negative overhangs it moves towards it. Figure 18 shows the variation of C_l and C_l/C_d with flap overhang. Both C_l and C_l/C_d show optima for each of the flap deviations considered. However, the variations are very small

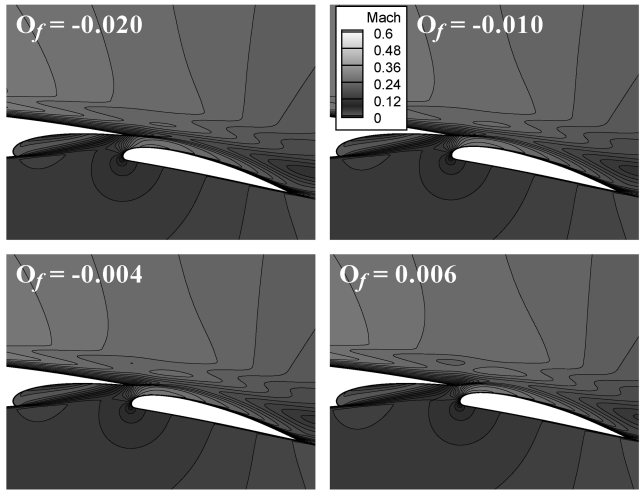

a) Mach contours through the flap slot at different flap overhangs (at $G_{f_{opt}}$)

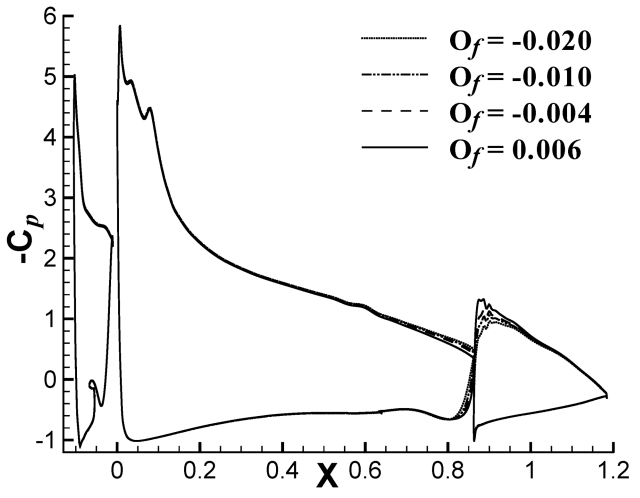

b) C_p at different O_f

Fig. 19 Development of the flow through the flap slot: $\delta_f = 20$ deg, $\delta_s = 25$ deg, $G_s = 0.021$, $O_s = -0.01$, $\alpha = 12$ deg, $M_\infty = 0.197$, and $Re = 3.52 \times 10^6$.

compared to the influence of the flap gap. Figure 19a shows the Mach number distribution around the flap for $\delta_f = 20$ deg and $\alpha = 12$ deg. We observe a general increase in Mach numbers through the flap slot as the overhang is increased. Unlike in the case of flap gap variation, increasing O_f at constant G_f does not cause the wakes from the forward elements to recede from the flap boundary layer. There is only a small gain in the flap suction peak and marginal variation of pressure on the main element; see Fig. 19b. Only a negligible effect is felt over the main element and the slat due to changing flap overhang.

Finally we investigate the effect of flap deviation (δ_f). The flap gap and flap overhang are set to $G_f = 0.025$ and $O_f = 0.0$, respectively. The lift increases with increasing flap deviation, which is expected because the flap is an aft element. Figure 20 presents the variation of C_l and C_l/C_d as a function of flap deviation at three different angles of attack: $\alpha = 0.00$, 4.01, and 12.00 deg. As δ_f is increased, the drag increases faster than the lift such that C_l/C_d achieves its optimum earlier than C_l for all angles of attack. Figure 21 shows the distribution of the Mach number around the flap and the slat for the settings: $\delta_f = 10$, 25, 34, and 40 deg, $G_f = 0.025$ and $\alpha = 4.01$ deg. At lower flap deviations, the jet through the flap slot flows all over the flap element confining the separation of the flap boundary layer near the trailing edge of the flap. As δ_f is increased, the accelerated jet through the flap slot reduces the extent of the main-element cove

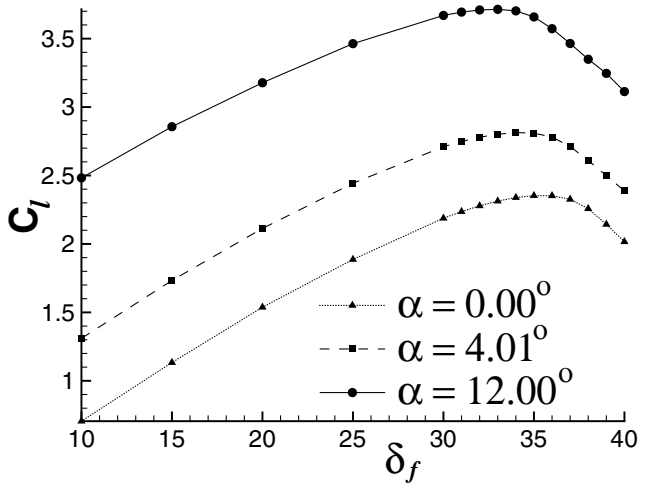

a) C_l vs flap deviation

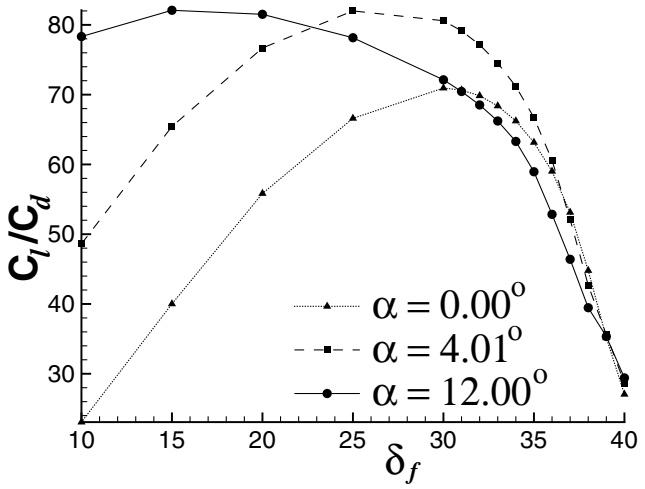

b) C_l / C_d vs flap deviation.

Fig. 20 Load coefficients as a function of the flap deviation at various α: $G_f = 0.025$, $O_f = 0$, $\delta_s = 25$ deg, $G_s = 0.021$, $O_s = -0.01$, $M_\infty = 0.197$, and $Re = 3.52 \times 10^6$.

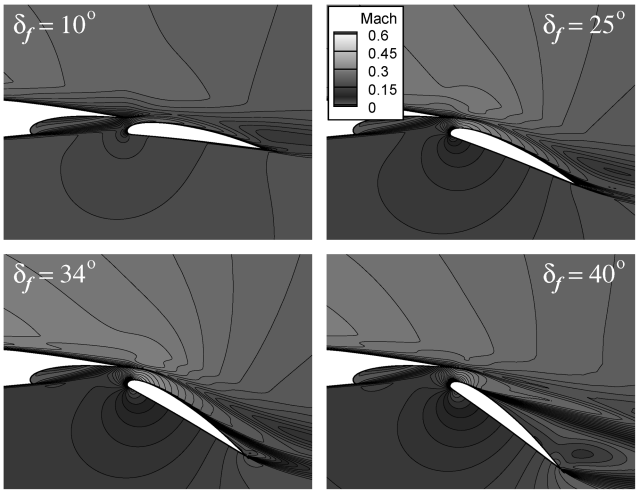

a) Mach contours through the flap slot

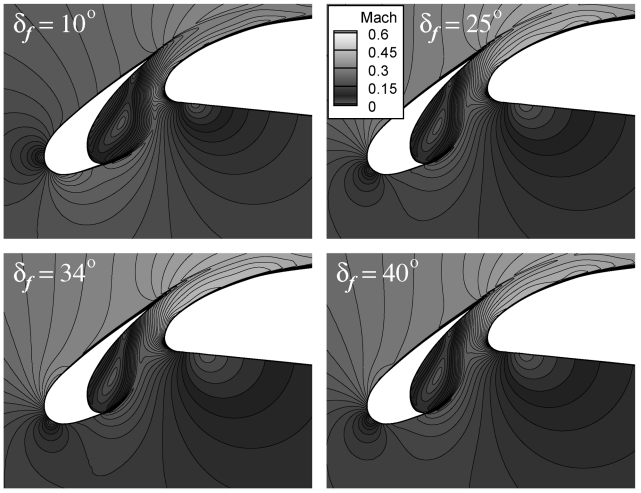

b) Mach contours through the slat slot

Fig. 21 Mach contours at different flap deviations: $G_f = 0.025$, $O_f = 0$, $\delta_s = 25$ deg, $G_s = 0.021$, $O_s = -0.01$, $\alpha = 4.01$ deg, $M_\infty = 0.197$, and $Re = 3.52 \times 10^6$.

vortex; see Fig. 21a. The relative orientation of the flap and the main element is such that the upwash of the jet speeding through the flap slot causes a suction which is felt significantly upstream all above the main element and the slat; see Fig. 22. As δ_f is increased further, the wakes from the forward elements flowing over the flap get offset. As a result, the separation of the flap boundary layer grows significantly, causing lift losses over the flap. Subsequently, the reduced upwash decreases the loading above the main element and the slat as well; see Fig. 22 as δ_f is increased from 34 to 40 deg.

We summarize the salient trends of the flow past the high-lift system due to changing flap riggings. At small and moderate deployments of the flap parameters, one can observe the following: 1) the flap gap affects the flap suction peak significantly whereas the flap overhang affects it marginally; 2) increasing the flap gap significantly reduces the loading underneath the main-element cove whereas increasing the flap overhang marginally enhances its contributions to total lift. At higher riggings though, flow separation over the flap drastically reduces the flap loading as well as the loading over the main element and the slat. This observation is consistent with the experimental study by Lin and Dominik [29]. Increasing the flap gap affects the flow over the main element and the slat to some extent whereas increasing the overhang has a marginal effect. In the present study, Figs. 16 and 18 and Tables 3 and 4 show maximum C_l at $\delta_f \approx 30$ deg for the intermediate angles of attack. At this flap deviation and $\alpha = 12$ deg, $C_{l_{\text{opt}}} = 3.74$ is achieved at $G_f = 0.015$

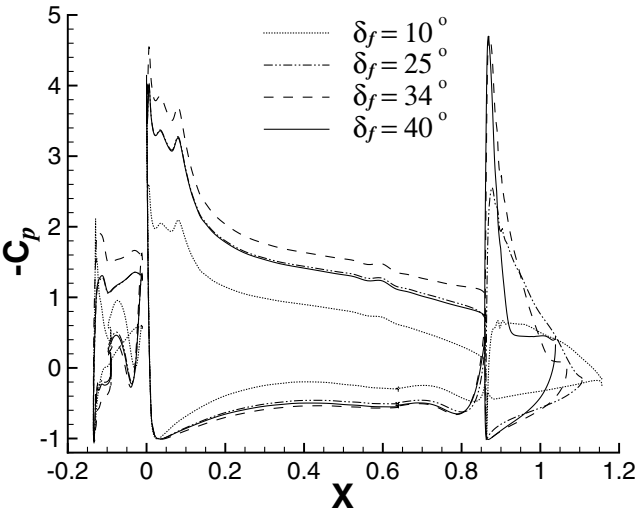

Fig. 22 C_p distribution for different flap deviations: $G_f = 0.025$, $O_f = 0$, $\delta_s = 25$ deg, $G_s = 0.021$, $O_s = -0.01$, $\alpha = 4.01$ deg, $M_\infty = 0.197$, and $Re = 3.52 \times 10^6$.

Table 4 Optimum flap overhangs at $G_{f_{opt}}$

δ_f	$O_{f_{opt}}$	$C_{l_{opt}}$	$(C_l/C_d)_{opt}$
15 deg	−0.4%	2.85	82.3
20 deg	−0.3%	3.18	82.0
25 deg	−0.3%	3.49	79.2
30 deg	−0.1%	3.74	74.5

($g_f = 0.010$) and $O_f \approx 0$. This is an 18% increase in lift over the reference configuration at $\alpha = 12$ deg. $(C_l/C_d)_{opt} = 82.3$ is achieved at $G_f = 0.023$ ($g_f = 0.014$) and $O_f = -0.004$. The drag continuously increases with flap deviation and hence one has to compromise between maximum lift and minimum drag for an optimal setting of flap riggings.

Concluding Remarks

Detailed computational results of a parametric study concerning slat and flap riggings of a 2-D high-lift system are presented. Each of the six design parameters studied, namely, the gaps, overhangs, and deviations of the flap and the slat ($G_s, G_f, O_s, O_f, \delta_s, \delta_f$) were found to result in optimum C_l and C_l/C_d amidst a range of their settings in practice. The gaps, overhangs, and deviations uniquely affect the flow through both the flap slot and the slat slot. Increasing the gap leads to an increased flux through either of the slots resulting in lift losses under the front element and gains above the rear element. These opposing factors lead to optimum aerodynamic coefficients. Changing the slat gap slightly affects the flow aft of it whereas changing the flap gap affects the flow over the forward elements considerably. Higher slat gaps incur huge losses of lift under the slat cove whereas higher flap gaps result in moderate losses of loading over the slat and the main element, though not over itself. Increasing the deviation considerably affects flow separation. At higher flap deviations, wakes from the forward elements recede from the flap boundary layer which leads to flow separation on the flap. The resulting upwash in combination with the flow separation on the flap reduces the loading over the entire high-lift system. Changing slat deviation, however, can delay the flow separation over the flap by means of interaction of the wake spreading from the slat with the flap boundary layer. Increasing the overhang at constant gap away from the main element (+ for the flap and − for the slat) affects the pressure distribution around the elements in the two slot regions in a contrasting way. Unlike in the case of gap effect, increasing the overhang leads to minor changes in the suction peak of the aft element. Overall, the variations in the loading observed due to change in the overhang are negligible in comparison with the influence of gaps and deviations. The optimum C_l and C_l/C_d are found to occur simultaneously with slat riggings. However the best setting of flap riggings turns out to be a compromise between maximum lift and minimum drag. Among the values of the slat parameters considered in this study, from takeoff up to approach conditions ($\alpha = 4$–12 deg), $(C_l/C_d)_{opt} = 83.2$ is found at $\delta_s = 25$ deg, $G_s = 1.7\%$, and $O_s = -1.3\%$ whereas $C_{l_{opt}} = 3.20$ is found at $\delta_s = 15$ deg, $G_s = 2.1\%$, and $O_f = -1.1\%$. In case of flap parameters (at the optimal slat parameters) $(C_l/C_d)_{opt} = 82.3$ is found at $\delta_f = 15$ deg, $G_f = 2.3\%$, and $O_f = -0.4\%$ whereas $C_{l_{opt}} = 3.75$ is found at $\delta_f = 30$ deg, $G_f = 1.5\%$, and $O_f = -0.1\%$.

Acknowledgements

This research work has been supported by the Deutsche Forschungsgemeinschaft (DFG) in the Collaborative Research Center SFB 401 "Flow Modulation and Fluid-Structure Interaction at Airplane Wings" of Rheinisch–Westfälische Technische Hochschule, Aachen University, Aachen, Germany.

References

[1] Moitra, A., "Issues in 2-D High-Lift CFD Analysis: A Review," AIAA Paper 2003-4072, June 2003.

[2] Smith, A. M. O., "High-Lift Aerodynamics," *Journal of Aircraft*, Vol. 12, No. 6, 1975, pp. 501–530.

[3] Cebeci, T., Chang, K. C., Clark, R. W., and Halsey, N. D., "Calculation of Flow Over Multielement Airfoils at High Lift," *Journal of Aircraft*, Vol. 24, No. 8, 1987, pp. 546–551.

[4] King, D. A., and Williams, B. R., "Developments in Computational Methods for High- Lift Aerodynamics," *Aeronautical Journal*, Vol. 92, No. 917, 1988, pp. 265–288.

[5] Rogers, S. E., Wiltberger, N. L., and Kwak, D., "Efficient Simulation of Incompressible Viscous Flow Over Single and Multielement Airfoils," *Journal of Aircraft*, Vol. 30, No. 5, 1993, pp. 736–743.

[6] Rogers, S. E., "Progress in High-Lift Aerodynamic Calculations," *Journal of Aircraft*, Vol. 31, No. 6, 1994, pp. 1244–1251.

[7] Shima, E., "Numerical Analysis of Multiple Element High-Lift Devices by Navier-Stokes Equation Using Implicit TVD Finite Volume Method," AIAA Paper 88-2574, June 1988.

[8] Chow, R., and Chu, K., "Navier-Stokes Solution for High-Lift Multielement Airfoil System with Flap Separation," AIAA Paper 91-1623, June 1991.

[9] Mavriplis, D. J., "Euler and Navier-Stokes Computation for Airfoil Geometries Using Unstructured Grids," *CASI Journal*, Vol. 36, No. 2, 1990, pp. 62–71.

[10] Baldwin, B. S., and Barth, T. J., "A One-Equation Turbulence Transport Model for High Reynolds Number Wall-Bounded Flows," AIAA Paper 91-0610, Jan. 1991.

[11] Spalart, P. R., and Allmaras, S. R., "A One-Equation Turbulence Model for Aerodynamic Flows," AIAA Paper 92-0439, Jan. 1992.

[12] Menter, F. R., "Zonal Two-Equation $k-\omega$ models for Aerodynamic Flows," AIAA Paper 93-2906, July 1993.

[13] Squire, L. C., "Interaction Between Wakes and Boundary Layers," *Progress in Aerospace Sciences*, Vol. 26, No. 3, 1989, pp. 261–288.

[14] Nelson, T. E., Zingg, D. W., and Johnston, G. W., "Compressible Navier-Stokes Computations of Multielement Airfoil Flows Using Multiblock Grids," *AIAA Journal*, Vol. 32, No. 3, 1994, pp. 506–511.

[15] Eyi, S., Lee, K. D., Rogers, S. E., and Kwak, D., "High-Lift Design Optimization Using Navier-Stokes Equations," *Journal of Aircraft*, Vol. 33, No. 3, 1996, pp. 499–504.

[16] Egami, K., Shima, E., Nakamura, S., and Amano, K., "Two-Dimensional Navier-Stokes Analysis of High-Lift Multi-Element Airfoils Using the $q-\omega$ Turbulence Model," AIAA Paper 93-0679, Jan. 1993.

[17] Mavriplis, D. J., "Multigrid Solution of Compressible Turbulent Flow on Unstructured Meshes Using a Two-Equation Model," AIAA Paper 91-0237, Aug. 1991.

[18] Godin, P., Zingg, D. W., and Nelson, T. E., "High-Lift Aerodynamic Computations with One- and Two-Equation Turbulence Models," *AIAA Journal*, Vol. 35, No. 2, 1997, pp. 237–243.

[19] Nield, B. N., "An Overview of the Boeing 777 High Lift Aerodynamic Design," *Aeronautical Journal*, Vol. 99, No. 989, 1995, pp. 361–371.

[20] Anderson, W. K., and Bonhaus, D. L., "Navier-Stokes Computations and Experimental Comparisons for Multielement Airfoil Configurations," AIAA Paper 93-0645, Jan. 1993.

[21] Nelson, T. E., Godin, P., Rango, S. D., and Zingg, D. W., "Flow Computations for a Three-Element Airfoil System," *Canadian Aeronautics and Space Journal*, Vol. 45, No. 2, 1999, pp. 132–139.

[22] Rumsey, C. L., Gatski, T. B., Ying, S. X., and Bertelrud, A., "Prediction of High-Lift Flows Using Turbulent Closure Models," AIAA Paper 97-2260, June 1997.

[23] Besnard, E., Schmitz, A., Boscher, E., Garcia, N., and Cebeci, T., "Two-Dimensional Aircraft High-Lift System Design and Optimization," AIAA Paper 98-0123, Jan. 1998.

[24] Besnard, E., Kural, O., and Cebeci, T., "Flow Predictions About Three-Dimensional High Lift Systems," AIAA Paper 99-0543, Jan. 1999.

[25] Nemec, M., and Zingg, D. W., "Newton-Krylov Algorithm for Aerodynamic Design Using the Navier-Stokes Equations," *AIAA Journal*, Vol. 40, No. 6, 2002, pp. 1146–1154.

[26] Kim, S., Alonso, J. J., and Jameson, A., "Design Optimization of High-Lift Configurations Using a Viscous Continuous Adjoint Method," AIAA Paper 2002-0844, Jan. 2002.

[27] Rai, M. M., "Robust Optimal Aerodynamic Design Using Evolutionary Methods and Neural Networks," AIAA Paper 2004-778, Jan. 2004.

[28] Quagliarella, D., and Vicini, A., "Airfoil and Wing Design Through Hybrid Optimization Strategies," *AIAA Journal*, Vol. 37, No. 5, 1999, pp. 634–641.

[29] Lin, J. C., and Dominik, C. J., "Parametric Investigation of a High-Lift Airfoil at High Reynolds Numbers," *Journal of Aircraft*, Vol. 34, No. 4, 1997, pp. 485–491.

[30] Moir, I., "Measurements on a Two-Dimensional Airfoil with High Lift Devices: A Selection of Experimental Test Cases for the Validation of CFD Codes," AGARD-AR-303, Aug. 1994.

[31] Rango, S. D., and Zingg, D. W., "Higher-Order Spatial Discretization for Turbulent Aerodynamic Computations," *AIAA Journal*, Vol. 39, No. 7, 2001, pp. 1296–1304.

[32] Fejtek, I., "Summary of Code Validation Results for a Multiple Element Airfoil Test Case," AIAA Paper 97-1932, June 1997.

[33] Rudnik, R., "Untersuchung der Leistungsfähigkeit von Zweigleichungs-Turbulenzmodellen bei Profilumströmungen," DLR-Forschungsbericht 97-49, 1997.

[34] Boucke, A., "Kopplungswerkzeuge für Aeroelastische Simulationen," Ph.D. Thesis, RWTH Aachen University, 2003.

[35] Bramkamp, F., "Unstructured *h*-Adaptive Finite-Volume Schemes for Compressible Viscous Fluid Flow," Ph.D. Thesis, RWTH Aachen University, 2003.

[36] Bramkamp, F. D., Lamby, P., and Müller, S., "An Adaptive Multiscale Finite Volume Solver for Unsteady and Steady State Flow Computations," *Journal of Computational Physics*, Vol. 197, 2004, pp. 460–490.

[37] Bramkamp, F. D., Gottschlich-Müller, B., Hesse, M., Lamby, P., Müller, S., Ballmann, J., Brakhage, K. H., and Dahmen, W., "*H*-Adaptive Multiscale Schemes for the Compressible Navier-Stokes Equations: Polyhedral Discretization, Data Compression and Mesh Generation," *Notes on Numerical Fluid Mechanics and Multidisciplinary Design*, Vol. 84, 1st ed., Springer, Berlin, 2003, pp. 125–204.

[38] Bramkamp, F. D., and Ballmann, J., "An Implicit Upwind Finite Volume Scheme for 3D Unstructured Meshes of Arbitrary Topology," *Proceedings of the WSEAS/IASME International Conference on Fluid Mechanics, Corfu*, Paper No. 488-366, 17–19 Aug. 2004.

[39] Batten, P., Leschziner, M. A., and Goldberg, U. C., "Average-State Jacobians and Implicit Methods for Compressible Viscous and Turbulent Flows," *Journal of Computational Physics*, Vol. 137, No. 1, 1997, pp. 38–78.

[40] Davis, S. F., "Simplified Second-Order Godunov-Type Methods," *SIAM Journal on Scientific and Statistical Computing*, Vol. 9, No. 3, 1988, pp. 445–473.

[41] Thomas, J. L., and Salas, M. D., "Far-Field Boundary Conditions for Transonic Lifting Solutions to the Euler Equations," *AIAA Journal*, Vol. 24, No. 7, 1986, pp. 1074–1080.

[42] Rumsey, C. L., Lee-Rausch, E. M., and Watson, R. D., "Three-Dimensional Effects in Multi-Element High Lift Computations," *Computers & Fluids*, Vol. 32, No. 5, 2003, pp. 631–657.